Effect of scatter correction on the compartmental measurement of striatal and extrastriatal dopamine D_2 receptors using [^{123}I]epidepride SPET

Masahiro Fujita[1, 2, 7], Andrea Varrone[1, 3], Kyeong Min Kim[4], Hiroshi Watabe[4], Sami S. Zoghbi[1, 2, 5], Nicholas Seneca[1, 2], Dnyanesh Tipre[2], John P. Seibyl[6], Robert B. Innis[1, 2], Hidehiro Iida[4]

[1] Department of Psychiatry, Yale University School of Medicine and VA Connecticut Healthcare System, West Haven, CT, USA
[2] Molecular Imaging Branch, National Institute of Mental Health, Bethesda, MD, USA
[3] Biostructure and Bioimaging Institute, National Research Council, Napoli, Italy
[4] Department of Investigative Radiology, National Cardiovascular Center Research Institute, Osaka, Japan
[5] Department of Radiology, Yale University School of Medicine and VA Connecticut Healthcare System, West Haven, CT, USA
[6] Institute for Neurodegenerative Disorders, New Haven, CT, USA
[7] Building 1, Room B3-10, MSC-0135, Bethesda, USA

Abstract. Prior studies with anthropomorphic phantoms and single, static in vivo brain images have demonstrated that scatter correction significantly improves the accuracy of regional quantitation of single-photon emission tomography (SPET) brain images. Since the regional distribution of activity changes following a bolus injection of a typical neuroreceptor ligand, we examined the effect of scatter correction on the compartmental modeling of serial dynamic images of striatal and extrastriatal dopamine D_2 receptors using [^{123}I]epidepride. Eight healthy human subjects [age 30±8 (range 22–46) years] participated in a study with a bolus injection of 373±12 (354–389) MBq [^{123}I]epidepride and data acquisition over a period of 14 h. A transmission scan was obtained in each study for attenuation and scatter correction. Distribution volumes were calculated by means of compartmental nonlinear least-squares analysis using metabolite-corrected arterial input function and brain data processed with scatter correction using narrow-beam geometry μ (SC) and without scatter correction using broad-beam μ (NoSC). Effects of SC were markedly different among brain regions. SC increased activities in the putamen and thalamus after 1–1.5 h while it decreased activity during the entire experiment in the temporal cortex and cerebellum. Compared with NoSC, SC significantly increased specific distribution volume in the putamen (58%, P=0.0001) and thalamus (23%, P=0.0297). Compared with NoSC, SC made regional distribution of the specific distribution volume closer to that of [^{18}F]fallypride. It is concluded that SC is required for accurate quantification of distribution volumes of receptor ligands in SPET studies.

Keywords: Nonlinear least-squares analysis – Ordered subsets expectation maximization – Putamen – Thalamus – Temporal cortex

Introduction

Analogous to comparable positron emission tomography (PET) studies, single-photon emission tomography (SPET) has been used to image neuroreceptors, transporters, and regional cerebral blood flow. In general, the data provided by SPET are not as accurate as those provided by PET owing to lower spatial resolution, lower sensitivity, depth dependency of attenuation, and a greater influence from scattered radiation. However, recent studies have shown that the accuracy of SPET quantification can be significantly improved by minimizing errors caused by these limitations. Attenuation correction in SPET is usually performed by determining the path length on an image after filtered back-projection instead of performing correction during iterative reconstruction. The latter more accurate and more computer-intensive method decreased errors compared with the former approximated method by 10–20% in the quantification of a brain phantom [1]. Differences in attenuation coeffi-

Masahiro Fujita (✉)
Molecular Imaging Branch, National Institute of Mental Health, Bethesda, MD, USA
e-mail: FujitaM@intra.nimh.nih.gov
Tel.: +1-301-4518898, Fax: +1-301-4803610

cients caused by heterogeneous distribution of tissues have been corrected by using a measured attenuation map (transmission scan). Although some image slices contain tissues with significantly different attenuation coefficients, in most areas in the head, attenuation is fairly uniform. Therefore, errors corrected by using a measured attenuation map were relatively small and on the order of 5% [2, 3, 4, 5].

Scatter correction provided greater improvement in accuracy, shown with anthropomorphic brain phantoms to be on the order of 30–70% [4, 6, 7]. In addition to phantom data, scatter correction in single, static in vivo SPET images of brain have shown comparable significant improvements in quantitation. In cerebral blood flow studies using [123I]iodoamphetamine, scatter correction improved image contrast by increasing and decreasing activities in gray and white matter, respectively [2, 8]. Scatter correction showed similar changes in dopamine D_2 receptor and transporter imaging studies, where the correction increased and decreased activities in the high-density (striatum) and background regions (cerebellum and occipital cortex), respectively [5, 6, 9].

[123I]Epidepride has high affinity for dopamine D_2 receptors and low nonspecific binding, which enables measurements in low-density receptor regions such as the thalamus and the temporal cortex [10]. This radioligand has been used to measure receptor occupancy of neuroleptics in schizophrenic patients [11] and receptor densities in extrastriatal areas in alcoholic patients [12]. The effect of scatter correction on this radioligand in single static images has been studied by comparing SPET and PET data obtained with 123I- and 11C-labeled epidepride, respectively [9]. SPET and PET activities were compared from a single target (striatum) and a single background (cerebellum) region at a few time points without calculating distribution volume or equilibrium ratios of specific-to-nondisplaceable binding. In fact, the half-life of 11C is too short to calculate the distribution volumes for this slowly equilibrating ligand. Fractions of scattered radiation in each region are affected by the distribution of activity in surrounding areas. Dynamic brain images acquired after bolus injection of a radioligand show varying relative distributions of brain activity as the ligand is delivered to and later washed from the brain.

The purpose of the current study was to examine the effect of a scatter correction method previously validated and shown to improve image accuracy [2, 6] on compartmental quantitation of dynamic SPET neuroreceptor imaging data in a background and three regions with variable receptor densities and locations (putamen, thalamus and temporal cortex). The study complied with the current laws of the USA, where it was performed, inclusive of ethics approval.

Materials and methods

Subjects. Data of eight [three males and five females; 30.1±8.3 (22–46) years of age; with these and subsequent values expressed as mean±SD (range)] among 11 subjects reported previously [13] were reanalyzed in this study. Two studies were excluded because a few data points of arterial input function were missing, and one study was excluded because the magnetic resonance imaging (MRI) scans were missing.

Data acquisition. Details of data acquisition have been described previously [13]. In brief, [123I]epidepride [373±12 (354–389) MBq, specific activity greater than 185 MBq/nmol in all syntheses] prepared locally was injected intravenously as a bolus and SPET data were acquired with a triple-headed camera with low-energy high-resolution fanbeam collimators (PRISM 3000XP, Philips Medical System, The Netherlands) for a duration of 13.9±0.6 (12.6–14.5) h after the injection. One transmission scan using a 57Co line source opposing head 3 of the camera was also acquired at approximately 2 h as previously described [3]. In this scan, both 57Co and 123I data were acquired simultaneously by opening two windows (simultaneous transmission emission protocol, STEP) to use the latter data to coregister the transmission to each emission data as described below. Arterial samples were obtained to measure metabolite-corrected input function. To identify brain regions, T1-weighted MRI scans of 3-mm contiguous slices were obtained with a 1.5-Tesla GE Signa device [13].

Attenuation map generation. The procedures of attenuation map generation have been described previously [6]. In brief, transmission projection data of head 3 were corrected for contamination of 123I emission photons and normalized by a blank projection. After smoothing with the Gaussian filter (kernel size = 3 pixels) to reduce noise, transmission data were reconstructed using the ordered subsets expectation maximization (OSEM) algorithm [14] to generate the attenuation map of narrow-beam geometry μ for 57Co. The attenuation map for 57Co was converted to that of narrow-beam μ for 123I by applying scaling factors [3].

Narrow-beam μ can be applied to compensate attenuation of photons for narrow-beam geometry, which allows, in theory, the detection of only primary photons [15]. In practice, however, a general SPET system has broad-beam geometry, because the collimator has an acceptance angle that allows the acquisition of not only the primary photons but also Compton-scattered photons. Therefore, the use of narrow-beam μ without scatter correction overcompensates photon absorption with a buildup factor caused by the broad-beam condition. To prevent this overcompensation, an attenuation map of broad-beam μ for reconstruction without scatter correction was obtained by applying a scaling factor to the attenuation map of narrow-beam μ [16]. Based on a study using an anthropomorphic calibration phantom (Radiology Support Device Inc., Long Beach, CA, USA) (Fig. 1), we set the scaling factor as 0.65 to produce an even horizontal profile across the transverse plane reconstructed without scatter correction [NoSC (broad) in Fig. 1]. If this factor of 0.65 was not applied for the data processing without scatter correction, an even horizontal profile was not obtained [NoSC (narrow) in Fig. 1]. An even horizontal profile was also obtained with scatter correction using narrow-beam μ attenuation maps (SC in Fig. 1). [123I]epidepride SPET data were analyzed with scatter correction using narrow-beam μ (SC) and without scatter correction using broad-beam μ attenuation maps (subsequently the latter data processing is simply referred to as NoSC).
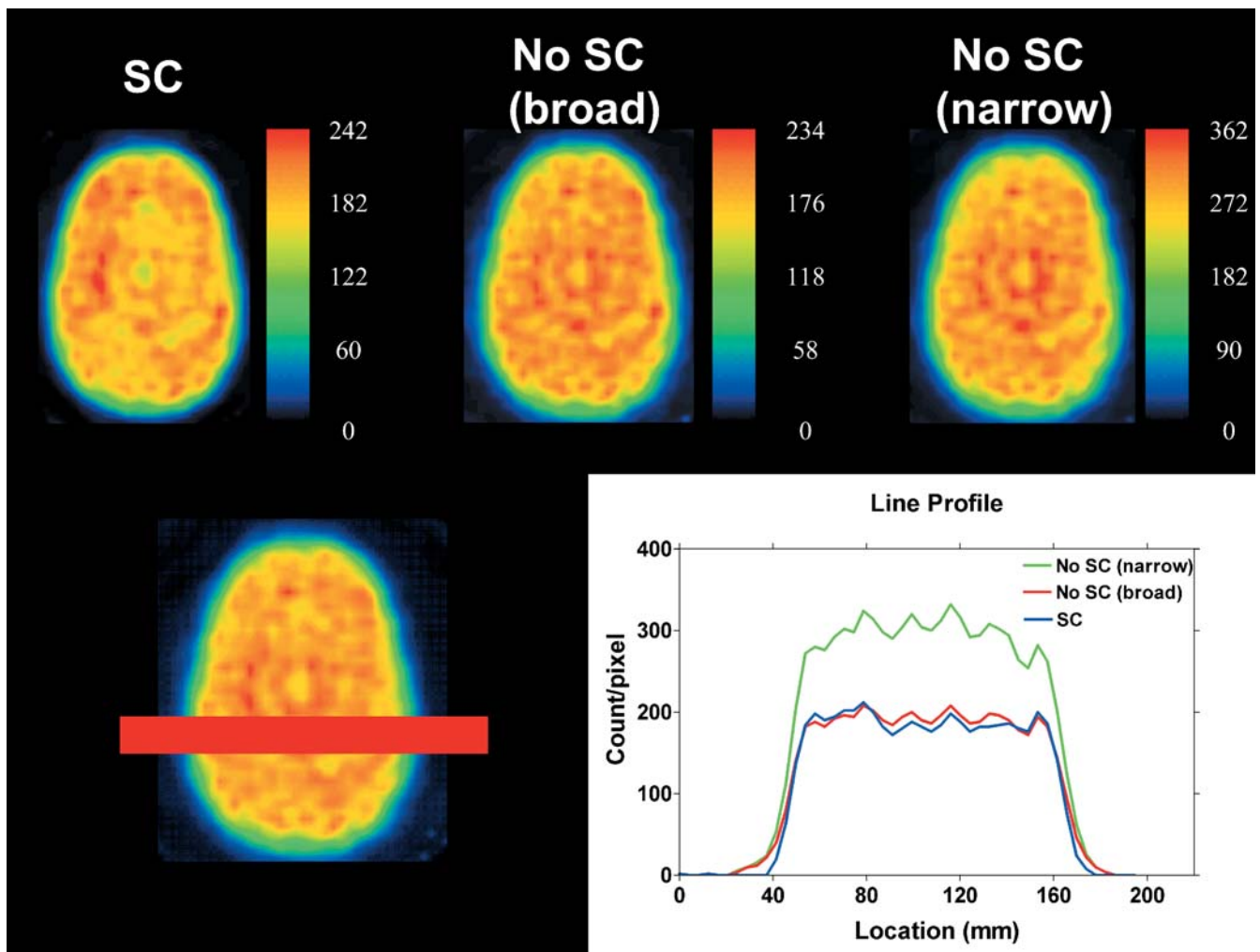
Fig. 1. Anthropomorphic phantom images reconstructed with scatter correction using narrow-beam geometry μ (*upper left, SC*), without scatter correction using broad-beam μ [*upper middle, NoSC (broad)*], and without scatter correction using narrow-beam μ [*upper right, NoSC (narrow)*]. Broad-beam μ values were 65% of narrow-beam μ (see text) so that the line profile is even (cf. the image in the lower row and the graph). Note that SC gave an even line profile but NoSC (narrow) did not. *Numbers on the color bars are counts/pixel*

Cross-calibration. SPET images of the brain phantom with uniform activity in the entire intracranial cavity were used to calculate a cross-calibration factor (CCF) for the relative sensitivity of the SPET scanner and the well-counter. Three acquisitions were performed on different days with a well-mixed ^{123}I solution of uniform activity [12.6±0.1 (12.5–12.6) kBq/ml]. CCF was 5.56 and 5.79 kBq/cps for SC and NoSC, respectively.

Scatter correction. Scatter correction was performed as described previously using the transmission-dependent convolution subtraction with the following formulae [2, 6]:

$$k(x,y) = 1 - \frac{1}{A - B \cdot t(x,y)^{\beta/2}} + k_0$$

$$g(x,y) = g_{obs}(x,y) - k(x,y) \cdot (g_{obs}(x,y) \otimes s)$$

$t(x,y)$ is the attenuation factor for pixel (x,y) derived from the transmission projection. A, B, β and k_0 are constants determined from a previous experiment [17]; A=2.3069, B=A−1, β=0.2926, and k_0=0.2203. The values $g(x,y)$ and $g_{obs}(x,y)$ are scatter-corrected and observed emission projection data, respectively. s is the scatter function given as the sum of Gaussian and exponential functions [18], and $\otimes$ denotes the convolution integral.

Image reconstruction. Calibration phantom and human data were reconstructed as described previously [6] using the OSEM algorithm with and without SC. In both cases, attenuation correction was performed using an attenuation map. The number of iterations and subsets for reconstruction without scatter correction was set to 3 and 12, respectively. The number of 3 for iterations was the minimum condition for reconstruction with 12 subsets to provide uniform ratios between the striatum and background of five striatum phantom datasets using an anthropomorphic phantom (Radiology Support Device Inc., Long Beach, CA, USA). In the reconstruction with SC, because SC induces a change in spatial resolution [5], we tried to find the parameter that would minimize the spatial resolution difference and set the number to 2 for iterations and 6 for subsets, respectively.

Coregistration of a transmission to each emission scan is described in detail below because this procedure was not required in the previous study [6] with one emission and one transmission scan. In human studies using [^{123}I]epidepride, emission images

with and without SC were reconstructed in the following way. First, each emission image, including the one acquired at the same time as the transmission (STEP acquisition), was reconstructed without either scatter or attenuation correction. The emission scan acquired with the transmission was coregistered to each emission image using the coregister function of Statistical Parametric Mapping version '99 (SPM 99) [19]. Each coregistration was visually confirmed by coincidence of fiducial markers between two emission images. Using the parameters obtained in these coregistrations, the transmission image was coregistered to each emission data and then emission data were reconstructed with attenuation correction and with or without SC using the coregistered transmission data. The software package Dr. View 4.0 (Asahi Kasei Information Systems Co. Ltd, Tokyo, Japan) was used to display the projection data.

Data analysis. Each emission image, reconstructed with attenuation correction and with or without SC, was transformed back to the coordinate of the STEP acquisition by inversely applying the parameters obtained in the coregistration procedure described above. Images acquired during the first 40 min were summed to create an image with good visualization of cerebral cortices. MR images of each subject were coregistered to this summed image using the coregister function of SPM 99. Both the coregistered MR and reconstructed emission images created with and without SC were transformed to the Montreal Neurological Institute brain space using SPM 99 by using the T1 MRI template and obtaining transformation parameters from the coregistered MR images.

Volumes of interest (VOIs) were placed on the average image from spatially normalized MR images of all subjects. VOIs were placed on the putamen, thalamus, temporal cortex, and cerebellum. The volume of these VOIs was 2.9, 5.5, 26.4, and 33.2 cm^3, respectively.

Total [$V_T'=K_1/k_2(1+k_3/k_4)$] and specific ($V_3'= K_1 k_3/k_2 k_4$) distribution volumes of [^{123}I]epidepride were calculated as reported previously [13] using parent ligand levels in arterial plasma as the input function by applying three- (two-tissue) and two- (one-tissue) compartment models in receptor regions and the cerebellum, respectively. K_1, k_2, k_3, and k_4 are rate constants describing ligand transport from arterial plasma to the nondisplaceable compartment in the brain, from the nondisplaceable compartment to the vasculature, from the nondisplaceable compartment to the specific binding compartment, and from the specific binding compartment to the nondisplaceable compartment, respectively. In this analysis, K_1/k_2 was first determined in the cerebellum and then nonlinear least squares fitting was performed in each receptor region by fixing the K_1/k_2 value to that obtained in the cerebellum. V_3' and V_T' are ratios of [specific binding]/[total (free + protein bound) parent in arterial plasma] and [total binding]/[total parent in arterial plasma] under equilibrium, respectively. In other words, V_3' is equal to $f_1 \times B_{max}/K_d$, where f_1 is the free fraction of the parent ligand and V_T' is a summation of distribution volume in all tissue compartments. Quantification of [^{123}I]epidepride is influenced by the activity of lipophilic metabolites, and the correct equilibrium ratio of specific-to-nondisplaceable binding (V_3'') cannot be calculated using the activity in the cerebellum [13, 20, 21]. However, to study effects of SC on quantification of neuroreceptor/transporter imaging in general, V_3'' was calculated by a reference tissue model using the cerebellum as a receptor-poor region [22]. Without the influence of lipophilic metabolites, V_3'' is an equilibrium ratio of [specific binding]/[free + nonspecific binding] in the brain. PMOD 2.50 [23] was used to calculate V_3', V_T', and V_3''.

Statistical analysis. The standard errors of nonlinear least-squares estimation for rate constants were given by the diagonal of the covariance matrix [24] and expressed as a percentage of the rate constants (coefficient of variation, %COV). In addition, %COV of K_1/k_2, V_3', and V_T' was calculated from the covariance matrix using the generalized form of the error propagation equation [25], where correlations among rate constants were taken into account. Results obtained by SC and NoSC were compared by two-tailed paired *t* test in each region using SAS 8.2 (Cary, NC, USA), and *P* values of <0.05 were considered significant.

Results

SC and NoSC methods showed different spatial distributions of activities that changed over time after bolus administration of [^{123}I]epidepride (Figs. 2, 3). SC generally showed greater changes from NoSC at later time points, when distribution of activities was more heterogeneous, than at early time points. During early periods (Fig. 2a, 0–36 min), cerebral cortex gray matter was clearly visible owing to the radioligand delivery by blood flow, although the receptor density in these regions was low (lower row in Fig. 2a). Gray matter was more clearly visible by SC because of the lower activity in white matter. As shown by line profiles, on each slice in Fig. 2a, the difference between SC and NoSC was small in high-activity areas while SC showed slightly lower activities in low-activity areas, indicating that SC slightly increased image contrast. At a later time point (Fig. 2b, 3 h), SC showed a greater increase in image contrast than at earlier time points, as indicated by the greater difference between high- and low-activity areas in line profiles. However, the effect of SC was different between high- (striatum) and low- (temporal cortex) density regions. Compared with NoSC, SC increased activity in the striatum. SC and NoSC showed similar activity in the temporal cortex while the former showed lower activity in the cerebellum (upper row in Fig. 2b).

In addition to two time points shown in Fig. 2, Fig. 3 displays changes in activities over time. As described below, each region showed different effects of SC, with the most prominent effects in the highest (putamen) and lowest (cerebellum) activity regions. SC changed the shape of the time-activity curve in the putamen by increasing activity significantly after 1 h and causing the peak uptake time to be later (Fig. 3a). In this region, SC and NoSC showed similar activities initially, when distribution of activity was more uniform, than during later periods. NoSC caused lower activity than SC during later periods, when the distribution of activities deviated more from uniformity. As a result, peak uptake time of SC determined by a single time point with the highest activity [256±103 (84–370) min] tended to be later than that of NoSC [158±124 (21–382) min, *P*=0.11]. SC also showed different effects between early (within 1–1.5 h) and later periods in the thalamus (Fig. 3b). However, the effect of SC was not so prominent as in the putamen.
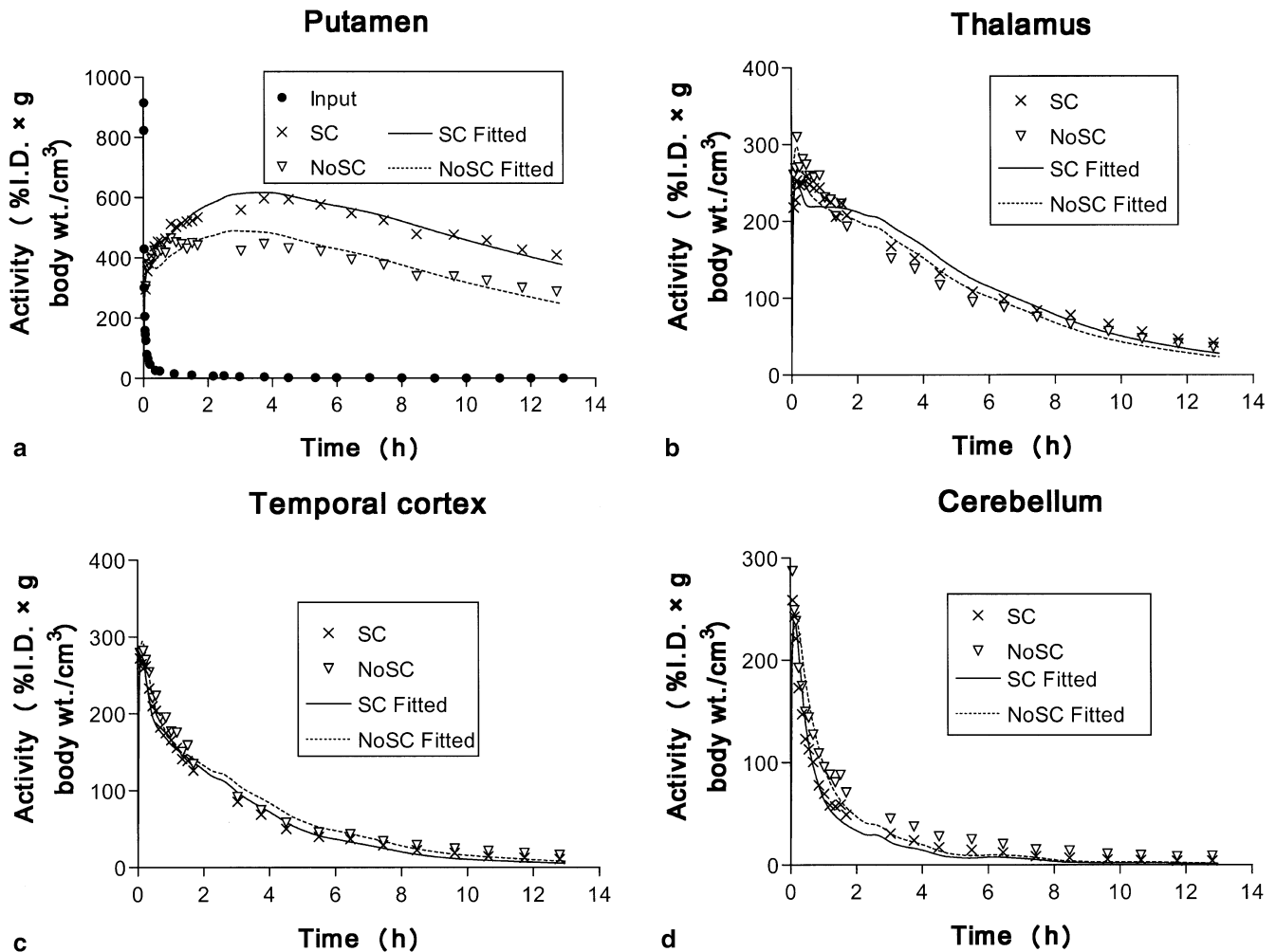
Putamen

Thalamus

Temporal cortex
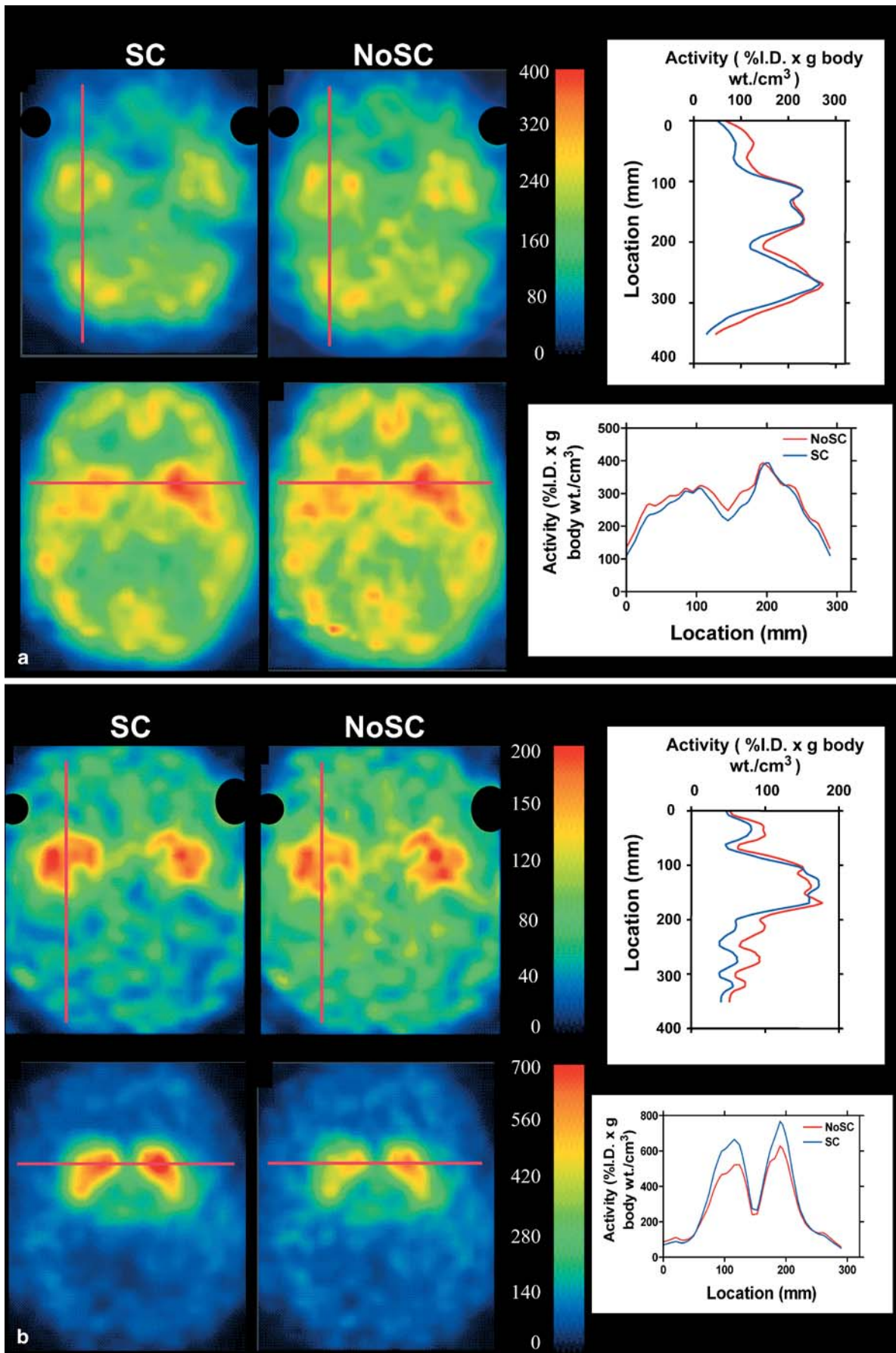
Cerebellum

Fig. 3a–d. Arterial input function (**a**) and changes in activity over time in the putamen (**a**), thalamus (**b**), temporal cortex (**c**), and cerebellum (**d**) obtained with scatter correction (*SC*) and no scatter correction (*NoSC*). Nonlinear least-squares fitting is also shown. See text for details

◄ **Fig. 2a, b.** Representative images reconstructed with scatter correction (*SC, left-hand column*) and without scatter correction using broad-beam μ (*NoSC, middle column*), and corresponding line profiles (*right-hand column*). Images on panels **a** and **b** were obtained at 0–36 and 172–192 min, respectively. The same slices normalized to the Montreal Neurological Institute brain space are shown in panels **a** and **b**. Activities of images, color bars and graphs are shown as percentages of injected dose per cm³ brain normalized to body weight in grams. If activity is evenly distributed throughout the body and is not excreted, the activity expressed in %I.D. × g body wt./cm³ is 100. The same intensity scale was applied to all images on panel **a**, and each of the upper and lower rows in panel **b**. See text for explanation of the effects of scatter correction. In the *upper rows*, radioactive fiducial markers attached to the skin were within the field of spatially normalized images. Because of the brightness of these markers relative to brain activity, they have been eliminated by placing black ellipses
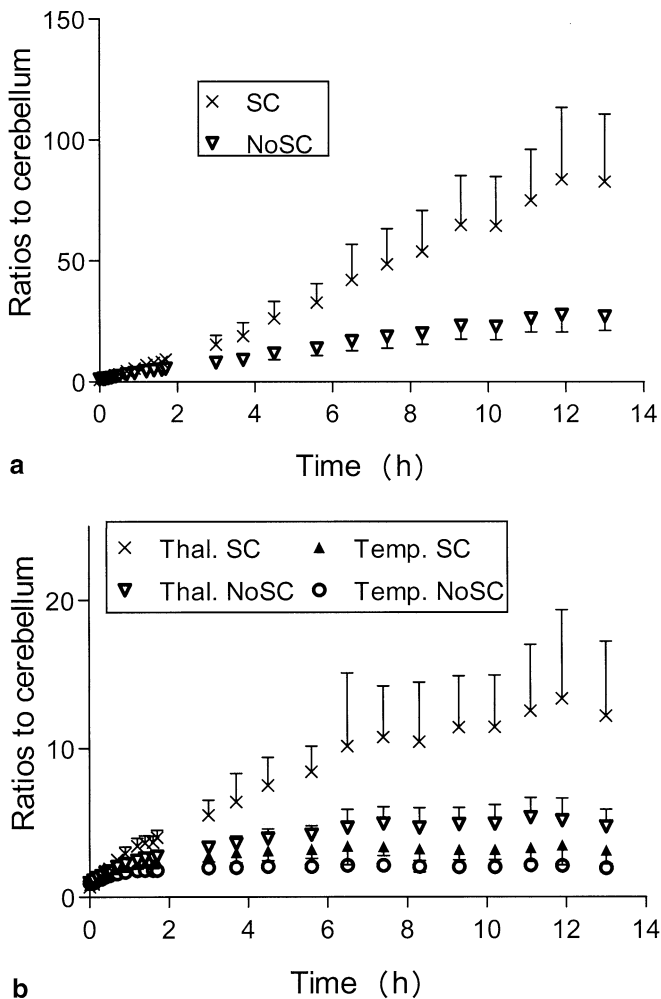
During early periods, activity of NoSC was higher than that of SC. In contrast, SC showed higher activity during later periods. As a result, peak uptake time of SC [32±19 (8–62) min] tended to be later than that of NoSC [20±12 (8–42) min, *P*=0.05]. In the cerebellum (Fig. 3d), SC decreased activity during almost the entire experiment, though to a greater extent at later time points. Results in the temporal cortex were similar to those in the cerebellum, with smaller effects of SC (Fig. 3c).

Ratios of activity in receptor regions to that in the cerebellum more clearly showed the different effects of SC among brain regions (Fig. 4). Data of all subjects are shown in this figure. Because SC decreased cerebellar activity significantly during the entire experiment, this method increased ratios in all three receptor regions. However, the magnitude and the time course of the increase differed among brain regions. The magnitude of the increase was in the order of receptor density, with the greatest increase in the putamen followed by the thalamus and the temporal cortex. The time course of the effect of SC also differed among brain regions. During late hours, in the putamen and the thalamus, the ratios obtained with SC increased more prominently than those obtained with NoSC, as shown by steeper slopes in the

Fig. 4a, b. Activity ratios of putamen (**a**) and thalamus (*Thal.*) and temporal cortex (*Temp.*) (**b**) to the cerebellum at each time point obtained with (*SC*) and without scatter correction (*NoSC*). Mean and SD (*error bars*) from all subjects are shown. Compared with NoSC, SC showed prominent increases in the ratios at late time points in the putamen and thalamus but not in the temporal cortex

Fig. 5a, b. Mean±SD values of the total (V_T') and specific (V_3') distribution volumes (**a**), and equilibrium ratios of specific-to-nondisplaceable binding (V_3'', **b**) obtained by scatter correction (*SC*) and no scatter correction (*NoSC*). *$P<0.005$; **$P<0.05$. *Put.*, Putamen; *Thal.*, thalamus; *Temp.*, temporal cortex; *Cbl.*, cerebellum

graphs, while such a difference between SC and NoSC was not apparent in the temporal cortex. This difference was caused because SC changed the shape of the time-activity curves and caused peak uptake times to be later in the putamen and thalamus but not in the temporal cortex and cerebellum.

Results of compartmental analysis are shown in Table 1 and Fig. 5. Because SC showed later peak and higher activity after 1–1.5 h in the putamen and the thalamus, it showed a trend toward smaller K_1 values, reflecting reduced delivery of the radioligand. On the other hand, these changes increased k_3/k_4 ratios (ratios of association to/dissociation from receptors) significantly. These changes induced by SC created greater V_T' values in these regions (Fig. 5a). Smaller activities with SC during almost the entire experiment provided smaller V_T'
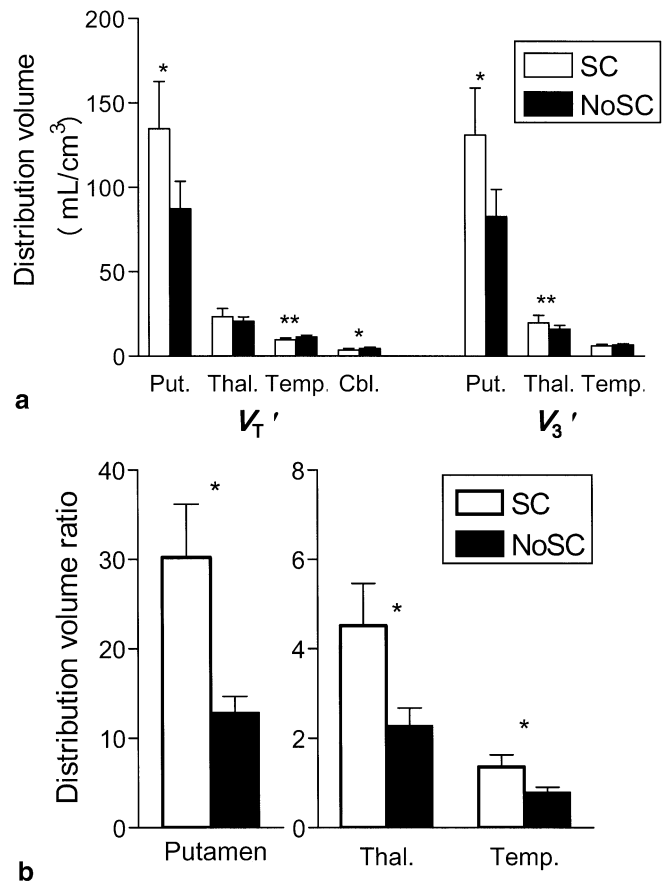
values in the temporal cortex and cerebellum. V_T' by SC was 134.7±28.0 (101.7–181.3), 23.4±4.9 (19.9–34.3), 9.8±1.0 (7.8–11.1), and 3.6±1.0 (2.7–5.6) ml/cm³ in the putamen, thalamus, temporal cortex, and cerebellum, respectively. Compared with NoSC, SC significantly increased V_T' in the putamen by 54.7% ($P=0.0002$). In contrast, SC decreased V_T' in the temporal cortex and cerebellum by 13.0% ($P=0.0187$) and 21.7% ($P=0.0011$), respectively. The increase in V_T' was not significant in the thalamus. V_3' with SC was 131.0±27.9 (98.7–177.1), 19.8±4.5 (16.5–30.1), and 6.2±0.9 (4.7–7.4) ml/cm³ in the putamen, thalamus, and temporal cortex, respectively. SC increased V_3' in the putamen and thalamus by 58.4% ($P=0.0001$) and 23.0% ($P=0.0297$), respectively (Fig. 5a). In the temporal cortex, the decrease in V_3' (7.5%) with SC was smaller than that in V_T' because in

Table 1. Rate constants and distribution volumes with scatter correction (narrow-beam μ) and no scatter correction (broad-beam μ)

	K_1 (ml cm^{-3} min^{-1})	K_1/k_2 (ml cm^{-3})	k_3 (min^{-1})	k_4 (min^{-1})	V_3' (ml cm^{-3})	V_T' (ml cm^{-3})
Scatter correction						
Putamen	0.44±0.20		0.087±0.038	0.0023±0.0006	131.0±27.9	134.7±28.0
	(7.7±2.8)		(8.7±4.8)	(11.2±5.5)	(4.8±1.9)	(4.7±1.8)
Thalamus	0.31±0.13		0.030±0.010	0.0054±0.0017	19.8±4.5	23.4±4.9
	(8.3±3.8)		(7.7±2.0)	(8.1±2.5)	(4.4±1.6)	(3.8±1.5)
Temp. cx.	0.31±0.11		0.017±0.006	0.0096±0.0014	6.2±0.9	9.8±1.0
	(6.0±2.0)		(9.2±1.5)	(9.7±1.3)	(4.9±1.2)	(3.1±0.8)
Cerebellum	0.31±0.13	3.6±1.0				
	(13.6±9.4)	(4.3±2.7)				
No scatter correction (broad-beam μ)						
Putamen	0.54±0.27		0.045±0.010	0.0025±0.0005	82.7±16.1	87.4±16.3
	(9.5±5.7)		(6.8±4.0)	(8.7±5.4)	(5.2±1.5)	(4.9±1.4)
Thalamus	0.38±0.17		0.021±0.002	0.0060±0.0009	16.1±2.2	20.7±2.5
	(7.5±3.5)		(8.1±2.0)	(8.8±2.1)	(4.7±1.1)	(3.7±0.9)
Temp. cx.	0.34±0.14		0.011±0.002	0.0077±0.0011	6.7±0.7	11.4±1.0
	(6.3±2.7)		(10.4±2.4)	(10.7±2.3)	(5.9±1.6)	(3.5±1.0)
Cerebellum	0.30±0.13	4.6±0.7				
	(18.8±12.0)	(6.2±3.9)				

Numbers in parentheses indicate identifiability of rate constants expressed as %COV

Temp. cx., Temporal cortex

this region and the cerebellum, SC showed changes in the same direction with greater magnitude in the latter. That is, the changes partially canceled out. Figure 5b shows V_3'' with and without SC. As expected from the increases in the ratios to the cerebellum at each time point (Fig. 4), SC increased V_3'' in all regions, with greater magnitude in higher density regions (Fig. 5b). The increase was 2.3, 2.0, and 1.7 times in the putamen, thalamus, and temporal cortex ($P<0.0001$ in all regions).

Discussion

A few groups have shown large effects of SC on SPET quantification, on the order of 30–70% [2, 4, 5, 6, 9]. However, these studies examined the effects of SC on static images or on only two regions. Thus, knowledge has been lacking on the effects of SC on quantification of distribution volumes with compartmental modeling for dynamic data, during which the regional distribution of activity changes in various brain regions with various densities. In this study, we examined the effects of SC on quantification of a dopamine D_2 receptor ligand, [123I]epidepride, which visualizes low-density regions such as the thalamus and the temporal cortex as well as a high-density region in the striatum. Our results showed markedly different effects of SC among these three regions and a receptor-poor region, the cerebellum. As shown previously [2, 6, 9], SC increased image contrast by increasing and decreasing activities in high- and low-

activity areas, respectively. However, the magnitude and time course of such changes varied significantly among brain regions.

Similar to the current work, another study using [123I]epidepride showed that SC caused increased and decreased striatal and cerebellar activities, respectively [9]. However, the magnitude of the changes cannot be compared to that in the current study because distribution volumes or equilibrium ratios of specific-to-nondisplaceable binding was not measured in that study. In fact, the authors of that paper suggested that the effect of SC on modeling analysis of the dynamic data should be examined in the future, which is the topic of the current paper. In the current study, in the putamen and thalamus, SC changed the shape of time-activity curves by increasing activities after 1–1.5 h and delaying the peak. Such changes decreased K_1, which reflects initial delivery of radioligand to brain regions, and increased k_3/k_4, which is a ratio of radioligand association to and dissociation from the receptor. In other words, SC provided kinetic rate constants indicating less initial delivery, faster association to, and slower dissociation from the receptor. These changes caused increases in V_3' ($=K_1 k_3/k_2 k_4$) in the putamen and thalamus (Fig. 5a). Although SC also increased k_3/k_4 in the temporal cortex, combined with the decreased K_1/k_2, SC did not change V_3' in this region. SC induced similar changes to V_3'' determined without arterial data (Fig. 5b) and k_3/k_4 determined by the compartmental analysis (Table 1). Both of these results reflected changes in the ratios of association to/dissociation from
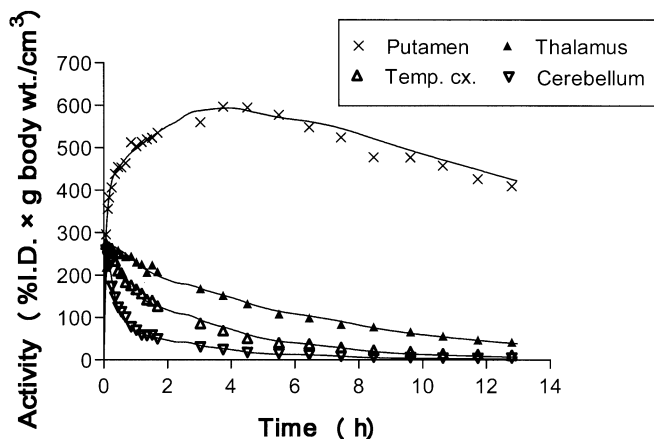
Fig. 6. Nonlinear least-squares fitting with an unconstrained two-compartment model for the scatter corrected data shown in Fig. 3. Note the significantly better fitting with the unconstrained two-compartment model. *Temp. cx.*, Temporal cortex. See text for details

receptors. The differences between V_3'' and k_3/k_4 were presumably caused by different sensitivity of the kinetic models to the noise of the data [26]. SC decreased activity in the cerebellum during almost the entire experiment, indicating that the influence of scattered radiation from other regions was prominent in this low-activity receptor-poor region (Fig. 3d). Such changes decreased the nondisplaceable distribution volume (K_1/k_2) in this region.

Our previous phantom and human studies also showed an increase and a decrease in activities in high- and low-activity regions, respectively [6]. It may be intuitively difficult to understand why SC increased activities in the putamen and thalamus compared with NoSC (Fig. 2a, b) although SC removed scattered radiation. The increase caused by SC occurred because narrow- and broad-beam geometry μ values were applied to SC and NoSC, respectively (see Materials and methods). A broad-beam μ map has values smaller than narrow-beam μ (in this study, narrow-beam μ was multiplied by 0.65) so as to create an even profile of a phantom image without applying SC (Fig. 1). Such an approximate method of compensating scattered radiation provides correct activities only for a uniformly distributed phantom, and errors become bigger as the distribution of activities deviates more from uniformity, as shown in our previous phantom study [6]. The current study showed greater effects of SC during late (Fig. 2b) than during early periods (Fig. 2a). These results are compatible with those in the phantom study because distribution of activities was more heterogeneous during late periods. If a region located centrally shows high activity and is surrounded by low-activity areas, such as the putamen, during late periods (Fig. 2b) there is a small influence of scattered radiation from the surrounding areas. However, NoSC, applying smaller than measured μ values, does not perform an

appropriate magnitude of attenuation correction and underestimates true activities (Fig. 3a). Such underestimation caused by the small μ values will be significant if the measured region is located centrally and there is a small influence from scattered radiation. On the other hand, SC applying measured μ values for attenuation correction and removing scattered radiation should provide activities closer to the true values. Therefore, compared with NoSC, SC should increase activities in a high-activity area surrounded by low activities, as seen in the putamen during late periods.

Striatal and extrastriatal dopamine D_2 receptors have been studied using a PET ligand, [18F]fallypride, which is a close analog of [123I]epidepride [27]. [18F]Fallypride showed B_{max}/K_d ratios of 9.1 for putamen/thalamus and 32.3 for putamen/temporal cortex [27]. Note that ratios of DVR−1 by their nomenclature are equal to ratios of B_{max}/K_d. In contrast, NoSC in the current study gave lower ratios of 5.1 for putamen/thalamus and 12.3 for putamen/temporal cortex (Table 1, Fig. 5a). SC analysis in the current study increased the ratios to 6.6 for putamen/thalamus and 21.2 for putamen/temporal cortex. These changes with SC and the results of our previous phantom study [6] indicate that SC significantly reduced errors in SPET measurement by reducing scattered radiation and that NoSC contained significant errors. However, other sources of errors in SPET measurement in the current study should be noted, e.g., lower spatial resolution, which would affect measurement in relatively small structures such as the putamen and thalamus, and lower sensitivity, which would affect measurement in low-count regions such as the temporal cortex and cerebellum.

For simplicity, in this study we applied the same constrained compartmental model that we applied previously and that was validated by comparison with equilibrium studies [13]. As described previously, goodness-of-fit was not good, particularly in the cerebellum. Another simple way to estimate V_3' without using a second input function is to subtract V_T' in the cerebellum from that in receptor-rich regions by assuming that the distribution volume of metabolites is uniform throughout the brain [28]. To confirm that the poor fitting did not cause biases in the difference between SC and NoSC, V_3' was calculated by applying an unconstrained two-tissue compartment model in all regions including the cerebellum (Fig. 6) and subtracting V_T' in the cerebellum from those in receptor-rich regions. The unconstrained model showed better fitting than the constrained model (Figs. 3 and 6). Compared with NoSC, SC showed similar changes in V_3' in the constrained (described above) and unconstrained models (see below). In the latter model, SC increased V_3' by 59% (*P*=0.0002) and 21% (*P*=0.0057) in the putamen and thalamus, respectively, and decreased V_3' by 13% in the temporal cortex (*P*=0.056). Therefore, the poor fitting did not cause biases in the differences in V_3' with SC and NoSC.

In summary, NoSC showed marked and variable errors of activities in brain regions. The magnitude and the direction of the errors were significantly different among putamen, thalamus, temporal cortex, and cerebellum. These differences were caused by the distribution of surrounding activity and the region's location (central vs peripheral). Broad-beam μ applied in NoSC decreased activity more in centrally located regions. Because of changing activity distributions in surrounding regions, the shape and peak time of the activity curve were altered, thereby changing the compartmental modeling results. Quantification of other imaging ligands will show varying errors in magnitude and direction, depending upon distribution, kinetics, and specific-to-nondisplaceable binding ratios. These errors will be particularly significant when studying both high- and low-density regions that are located in both central and peripheral regions of the brain, such as cortices, basal ganglia, thalamus and the hypothalamus, because such studies carry two layers of error source: (1) time course of the activity determined by receptor density and affinity of the ligand and (2) location. SC appears to be a prerequisite for accurate receptor quantification with SPET.

References

1. Kauppinen T, Koskinen MO, Alenius S, Vanninen E, Kuikka JT. Improvement of brain perfusion SPET using iterative reconstruction with scatter and non-uniform attenuation correction. Eur J Nucl Med 2000; 27:1380–1386.

2. Iida H, Narita Y, Kado H, Kashikura A, Sugawara S, Shoji Y, Kinoshita T, Ogawa T, Eberl S. Effects of scatter and attenuation correction on quantitative assessment of regional cerebral blood flow with SPECT. J Nucl Med 1998; 39:181–189.

3. Rajeevan N, Zubal IG, Ramsby SQ, Zoghbi SS, Seibyl J, Innis RB. Significance of nonuniform attenuation correction in quantitative brain SPECT imaging. J Nucl Med 1998; 39:1719–1726.

4. Stodilka RZ, Kemp BJ, Msaki P, Prato FS, Nicholson RL. The relative contributions of scatter and attenuation corrections toward improved brain SPECT quantification. Phys Med Biol 1998; 43:2991–3008.

5. Hashimoto J, Sasaki T, Ogawa K, Kubo A, Motomura N, Ichihara T, Amano T, Fukuuchi Y. Effects of scatter and attenuation correction on quantitative analysis of beta-CIT brain SPET. Nucl Med Commun 1999; 20:159–165.

6. Kim KM, Varrone A, Watabe H, Shidahara M, Fujita M, Innis RB, Iida H. Contribution of scatter and attenuation compensation to SPECT images of non-uniformly distributed brain activities. J Nucl Med 2003; 44:512–519.

7. Soret M, Koulibaly PM, Darcourt J, Hapdey S, Buvat I. Quantitative accuracy of dopaminergic neurotransmission imaging with (123)I SPECT. J Nucl Med 2003; 44:1184–1193.

8. Ito H, Iida H, Kinoshita T, Hatazawa J, Okudera T, Uemura K. Effects of scatter correction on regional distribution of cerebral blood flow using I-123-IMP and SPECT. Ann Nucl Med 1999; 13:331–336.

9. Almeida P, Ribeiro MJ, Bottlaender M, Loc'h C, Langer O, Strul D, Hugonnard P, Grangeat P, Maziere B, Bendriem B. Absolute quantitation of iodine-123 epidepride kinetics using single-photon emission tomography: comparison with carbon-11 epidepride and positron emission tomography. Eur J Nucl Med 1999; 26:1580–1588.

10. Kessler RM, Mason NS, Votaw JR, Depaulis T, Clanton JA, Ansari MS, Schmidt DE, Manning RG, Bell RL. Visualization of extrastriatal dopamine D_2 receptors in the human brain. Eur J Pharmacol 1992; 223:105–107.

11. Bressan RA, Erlandsson K, Jones HM, Mulligan RS, Ell PJ, Pilowsky LS. Optimizing limbic selective D_2/D_3 receptor occupancy by risperidone: A [123I]-epidepride SPET study. J Clin Psychopharmacol 2003; 23:5–14.

12. Kuikka JT, Repo E, Bergstrom KA, Tupala E, Tiihonen J. Specific binding and laterality of human extrastriatal dopamine D_2/D_3 receptors in late onset type 1 alcoholic patients. Neurosci Lett 2000; 292:57–59.

13. Fujita M, Seibyl JP, Verhoeff NPLG, Ichise M, Baldwin RM, Zoghbi SS, Burger C, Staley JK, Rajeevan N, Charney DS, Innis RB. Kinetic and equilibrium analyses of [123I]epidepride binding to striatal and extrastriatal dopamine D_2 receptors. Synapse 1999; 34:290–304.

14. Hudson HM, Larkin RS. Accelerated image reconstruction using ordered subsets of projection data. IEEE Trans Med Imaging 1994; 13:601–609.

15. Sorensen JA, Phelps ME. Physics in nuclear medicine. Philadelphia: Saunders, 1987.

16. Jaszczak RJ, Coleman RE, Whitehead FR. Physical factors affecting quantitative measurements using camera-based single photon emission computed tomography (SPECT). IEEE Trans Nucl Sci 1981; 28:69–80.

17. Kim KM, Watabe H, Shidahara M, Ishida Y, Iida H. SPECT collimator dependency of scatter and validation of transmission-dependent scatter compensation methodologies. IEEE Trans Nucl Sci 2001; 48:689–696.

18. Narita Y, Eberl S, Iida H, Hutton BF, Braun M, Nakamura T, Bautovich G. Monte Carlo and experimental evaluation of accuracy and noise properties of two scatter correction methods for SPECT. Phys Med Biol 1996; 41:2481–2496.

19. Friston KJ, Ashburner J, Poline JB, Frith CD, Heather JD, Frackowiak RSJ. Spatial registration and normalisation of images. Human Brain Mapping 1995; 2:165–189.

20. Ichise M, Fujita M, Seibyl JP, Verhoeff NP, Baldwin RM, Zoghbi SS, Rajeevan N, Charney DS, Innis RB. Graphical analysis and simplified quantification of striatal and extrastriatal dopamine D_2 receptor binding with [123I]epidepride SPECT. J Nucl Med 1999; 40:1902–1912.

21. Bergstrom KA, Yu M, Kuikka JT, Akerman KK, Hiltunen J, Lehtonen J, Halldin C, Tiihonen J. Metabolism of [123I]epidepride may affect brain dopamine D_2 receptor imaging with single-photon emission tomography. Eur J Nucl Med Mol Imaging 2000; 27:206–208.

22. Ichise M, Ballinger JR, Golan H, Vines D, Luong A, Tsai S, Kung HF. Noninvasive quantification of dopamine D_2 recep-

tors with iodine-123-IBF SPECT. J Nucl Med 1996; 37: 513–520.

23. Burger C, Mikolajczyk K, Grodzki M, Rudnicki P, Szabatin M, Buck A. JAVA tools quantitative post-processing of brain PET data. J Nucl Med 1998; 39:277P.

24. Carson RE. Parameter estimation in positron emission tomography. In: Phelps ME, Mazziotta JC, Schelbert HR, eds. Positron emission tomography and autoradiography: principles and applications for the brain and heart. New York: Raven; 1986: 347–390.

25. Bevington PR, Robinson DK. Data reduction and error analysis for the physical sciences. New York: McGraw-Hill, 2003.

26. Ichise M, Toyama H, Innis RB, Carson RE. Strategies to improve neuroreceptor parameter estimation by linear regression analysis. J Cereb Blood Flow Metab 2002; 22:1271–1281.

27. Mukherjee J, Christian BT, Dunigan KA, Shi B, Narayanan TK, Satter M, Mantil J. Brain imaging of ^{18}F-fallypride in normal volunteers: blood analysis, distribution, test-retest studies, and preliminary assessment of sensitivity to aging effects on dopamine D-2/D-3 receptors. Synapse 2002; 46:170–188.

28. Carson RE, Wu Y, Lang L, Ma Y, Der MG, Herscovitch P, Eckelman WC. Brain uptake of the acid metabolites of F-18-labeled WAY 100635 analogs. J Cereb Blood Flow Metab 2003; 23:249–260.